Flexible and efficient perovskite quantum dot solar cells *via* hybrid interfacial architecture

Long Hu
University of New South Wales

Qian Zhao
Nankai University

Shujuan Huang
Macquarie University

Jianghui Zheng
University of New South Wales   https://orcid.org/0000-0001-5123-7364

Xinwei Guan
King Abdullah University of Science and Technology

Robert Patterson
University of New South Wales

Jijun Kim
University of New South Wales

Lei Shi
University of New South Wales

Lei Qi
University of New South Wales

Chun-Ho Lin
University of New South Wales   https://orcid.org/0000-0003-0882-4728

Dewei Chu
The University of New South Wales

Tao Wan
University of New South Wales

Soshan Cheong
UNSW Sydney   https://orcid.org/0000-0001-6133-0829

Richard Tilley
UNSW Australia   https://orcid.org/0000-0003-2097-063X

Anita Ho-Baillie
The University of Sydney   https://orcid.org/0000-0001-9849-4755

Joseph Luther
National Renewable Energy Laboratory   https://orcid.org/0000-0002-4054-8244

Jianyu Yuan (✉ jyyuan@suda.edu.cn)

Soochow University

Tom Wu

UNSW Sydney

Article

Abstract

All-inorganic CsPbI3 perovskite quantum dots (QDs) have received intense research interest for photovoltaic applications because of the recently demonstrated higher power conversion efficiency compared to solar cells using other QD materials. These QD devices also exhibit good mechanical stability amongst various thin-film photovoltaic technologies. In this work, through developing a hybrid interfacial architecture consisting of CsPbI3 QD/PCBM heterojunctions, we report the formation of an energy cascade for efficient charge transfer at both QD heterointerfaces and QD/electron transport layer interfaces. The champion CsPbI3 QD solar cell has a best power conversion efficiency of 15.1%, which is among the highest report to date. Building on this strategy, we demonstrate the very first perovskite QD flexible solar cell with a record efficiency of 12.3%. A detailed morphological characterization reveals that the perovskite QD film can better retain structure integrity than perovskite bulk thin-film under external mechanical stress. This work is the first to demonstrate higher mechanical endurance of QD film compared to bulk thin-film, and highlights the importance of further research on high-performance and flexible optoelectronic devices using solution-processed QDs.

Introduction

Colloidal quantum dots (QDs) have received remarkable research attention due to their excellent properties such as tuneable bandgaps, multiple exciton effects and excellent stability[1–8]. These unique features facilitate their wide applications in optoelectronic devices such as photodetectors,[9–12] light emitting diodes[13–14] and photovoltaics[15–17]. Solution-processed QDs have demonstrated their strong potential for high-efficiency and low-cost photovoltaics. The best PbS QD solar cell has achieved a power conversion efficiency (PCE) of 13.8% due to improvements in surface passivation and device structure[18]. More recently, all-inorganic CsPbI$_3$ QDs have emerged as a rising star for photovoltaic applications because of their outstanding properties including phase stability that is otherwise not achievable in bulk thin-film form, and high photoluminescence (PL) quantum yields due to impressive defect tolerance[19–22]. Advances in CsPbI$_3$ QD solar cells have enabled high efficiency over 15% to be achieved, showing great potential for photovoltaics[23–24]. Importantly, fabrication of perovskite QDs involve colloidal synthesis and processing using industrially friendly solvents at room temperature, opening a new platform for developing high performance QD optoelectronic devices[25–29].

In addition, QD materials have been widely recognised to offer superior mechanical flexibility because of the intrinsic nanoscale dimensions[30–31]. Unfortunately, there is barely any experimental evidence proving their mechanical endurance relative to thin-films, especially for efficient flexible photovoltaics. We believe that there are two major merits that flexible QD devices can offer. One is high-quality QD film can be deposited at room temperature, which is ideal for all kinds of flexible substrates[32–35]. The other is QDs can deliver an excellent power-per-weight output, which is significant for lightweight and portable devices, or even spacecraft[36]. Although previous studies have demonstrated excellent flexural endurance of QD photovoltaics,[37–38] none have demonstrated high PCEs, probably due to poor charge transfer and carrier

extraction efficiencies at QD heterointerfaces and interfaces. PCEs of flexible QD photovoltaics have been limited to below 10%,[38] which lag significantly behind flexible organic and thin-film perovskite solar cells[39−40].

In this work, we have overcome these limitations demonstrating efficient flexible QD photovoltaics using emerging $CsPbI_3$ perovskite QDs. Taking advantage of extremely high surface areas of QDs, we developed a thin hybrid interfacial architecture (HIA) by introducing organic small molecules (phenyl-C61-butyric acid methyl ester (PCBM)) into the $CsPbI_3$ QD structure. The PCBM bonds with the under-coordinated Pb^{2+} ions on the QD surfaces through functional carboxyl groups, and creates an exciton cascade between the electron transport layer (ETL) SnO_2 and the $CsPbI_3$ QD layer, thus enabling efficient energy transfer and also promoting exciton dissociation at both QD heterointerfaces and QD/ETL interfaces. Using this HIA strategy, we achieve a champion PCE of 15.1%. In addition, we demonstrate the first flexible QD solar cell using these emerging perovskite QDs with a record efficiency of 12.3% as well as the improved mechanical operation stability in comparison with their bulk thin-film counterpart confirmed by detailed morphological characterization.

Results

PCBM/$CsPbI_3$ QD hybrid film

$CsPbI_3$ QDs were synthesized and purified according to the procedures previously published[19]. PCBM was added into the $CsPbI_3$ QDs dispersed in chlorobenzene (CB) to obtain a hybrid solution. The $CsPbI_3$ QDs with and without PCBM have similar cubic shape with an average size of about 10 nm, characterized by the transmission electron microscopy (TEM) shown in Fig. S1. **Fig. 1a** depicts two different kinds of QD film deposition and solid-state ligand removal process. In general, the QD solution was spin-coated onto a substrate under ambient conditions with low relative humidity (RH<10%) at room temperature. Then the native long oleic acid (OA) and oleylamine (OLA) ligands were removed by soaking the as-cast QD film in anhydrous methyl acetate (MeOAc)[20]. This procedure was repeated 3-5 times to build up ~300 nm thick films, resulting one control $CsPbI_3$ QD film and another hybrid PCBM/$CsPbI_3$ QD film.

We first comprehensively characterized the properties of $CsPbI_3$ QD films with or without PCBM using the Fourier transform infrared (FTIR), femtosecond transient absorption (fs-TA) and PL spectroscopy. In the FTIR spectra (**Fig. 1b**), the signal intensities of C-H modes at 2851 and 2921 cm^{-1} for both control and hybrid films were remarkably reduced comparing to the pristine film (without MeOAc treatment), which indicates the majority of native long chain ligands were removed after the MeOAc treatment and the addition of PCBM into the QD matrix had little effect on the process of surface ligand removal. To investigate the charge transfer dynamics in control and hybrid QD films, fs-TA measurements were carried out to collect the detailed information for both radiative and nonradiative processes[41-42]. As shown in **Fig. 1c-d**, the hybrid film exhibits more obvious bleaching shifts as increasing delay time than the control one, demonstrating the charge transfer occurs in hybrid film is under a stronger drive. The

corresponding time-resolved components extracted from the dynamic curves at bleaching peak of around 670 nm are shown in **Fig. 1e**. The time constants τ_1, τ_2 and τ_3 calculated through a three-exponential fitting are generally attributed to the hot phonon bottleneck, the Auger recombination and charge transfer process, respectively.[41] Clearly, the reduced charge transfer time in the hybrid film (312.8 ps) indicates more efficient charge extraction compared with that in the control film (483.2 ps). The slightly longer Auger recombination process in the hybrid film (57.6 ps *vs.* 52.3 ps) suggests less trap density, which possibly results from the passivation of PCBM.

Steady-state PL and time-resolved PL (TRPL) measurements were used to confirm the improved carrier dynamics observed in fs-TA measurements. As shown in Fig. S2, compared to the pristine film, the control QD film exhibits red-shifted PL peak with reduced intensity, indicating improved electronic coupling after surface ligand removal[41]. Meanwhile, the PCBM/CsPbI$_3$ QD hybrid film demonstrates obvious PL quenching with more red shift, suggesting the charge transfer between PCBM and CsPbI$_3$ QDs,[22, 32] and the further enhanced electron coupling in the hybrid blends. In addition, the faster PL decay profile (Fig. S3) for the hybrid CsPbI$_3$ QD indicates PCBM in the hybrid QD film could provide an effective transport channel for accelerating charge extraction, which is also consistent with the fs-TA analysis.

Performance of CsPbI$_3$ QD photovoltaics

The schematic diagrams of the control and the target PCBM/CsPbI$_3$ QD solar cell architectures are given in **Fig. 2a-b**, respectively. To fabricate the control devices without hybrid films, an ultra-thin PCBM was prepared on top of the SnO$_2$ layer. Each layer of both devices is clearly identified in the cross-sectional SEM image presented in Fig. S4. To achieve the best optimized PV performance, as shown in Table S1, we first tuned the thickness of the QD absorber layer for control QD devices. A decent efficiency of 12.4% is obtained using four depositing cycles. Then we optimized the thickness of the hybrid QD layer in the HIA, concluding the device with the 1:4 thickness ratios of hybrid QD layers to control QD layers delivered a highest efficiency up to 15.1%, which is among the highest reported efficiency for CsPbI$_3$ QD solar cells (Table S2). As shown in **Fig. 2c** and **Table 1**, the enhancement of PCE mainly contributed from the significantly improved short-circuits current density (J_{sc}). External quantum efficiency (EQE) was then carried out on the optimal control and target devices, showing the EQE of the target QD device is enhanced across the entire response region (**Fig. 2d**), which could result from the improved charge collection efficiency through introducing HIA. Furthermore, we increased the thickness of hybrid QD layers as the control QD layers without any change. The device having thicker hybrid QD layers exhibits decreased efficiency down to 13.8% (Table S1) that could be mainly resulted from the unfavourable effects of CB solvent during upper hybrid layer deposition,[43] leading to PCBM exfoliation from CsPbI$_3$ QDs in the bottom layer.

It should be noted that the HIA modification also leads to reduced *J-V* hysteresis (Fig. S5). The stabilized power output (SPO) of 14.61% for the target device and 11.93% for the control device were recorded (**Fig. 2d**), confirming the reliability of *J-V* measurements. We also characterized device stability (Fig. S6), and

found that the control device lost 50% of its initial efficiency while the target device degraded by only 30% after storage in dry air-filled box for 14 days, indicating that the HIA is also beneficial for improving device stability. The contact angle of water drop on control and hybrid film is presented in Fig. S7, indicating the hybrid film has a more hydrophobic nature, which is beneficial for improved the device stability as well as depositing the upper QD layer.

To understand the enhancements of QD photovoltaic performances, a series of device characterizations were further performed. Electrochemical impedance spectroscopy (EIS) is introduced to investigate the quality of interfaces. As shown in Fig. S8, the target device exhibits a similar series resistance (R_s=28.5 Ω) but a larger recombination resistance (R_{sh}=3346 Ω) than that of the control device, indicative of enhanced charge transfer and reduced charge recombination process. Additionally, their different dark J-V characteristics in Fig. S9 show that the target device exhibits a lower leakage current under reverse bias compared to the control device, indicating decreased carrier recombination. Furthermore, transient photocurrent and photovoltage (Fig. S10) were performed on both devices. The target device has longer lifetime of 65 μs compared to that of 59 μs in the control one, indicating a smaller charge recombination rate. The transient photovoltage exhibits a similar trend and the target device has a longer lifetime of 4.6 μs (3.6 μs for the control one), demonstrating a faster charge transport rate. All these results indicate the intrinsic mechanism of enhancement of QD photovoltaic performance lies in the improvement of the QD/ETL interfaces, which is attributed to the improved energy level alignment. The values of valence band (VB) energy level were characterized by ultraviolet photoelectron spectroscopy (UPS) (Fig. S11), and their conduction bands (CB) were further calculated according to their optical bandgaps (Fig. S11). As shown in **Fig. 2e-f,** PCBM has the appropriate electron affinity serving as a modification layer between the SnO_2 and the $CsPbI_3$ QDs, which leads to the suppressed charge recombination at the interface between SnO_2 and the $CsPbI_3$ QD layer. The efficient charge transfer in hybrid device is enabled by the formation of a gradient CB alignment that efficiently injects the photogenerated electrons into the CB of PCBM and then extracted to the SnO_2 ETL, as evidenced by the fs-TA and PL measurements. Hence, PCBM could be seen as a fast electron transport channel in the target QD device, which leads to the improved device performance.

$CsPbI_3$ QD-PCBM molecular interaction

To further understand the molecular interaction between $CsPbI_3$ QD and PCBM, density functional theory (DFT)-based molecular dynamic simulation and X-ray photoelectron spectrum (XPS) measurements were carried out. First, surface defects in the perovskite may lead to trap states that not only impede charge transport between the light absorber and the PCBM but also increase unfavorable interfacial recombination[44-45]. As shown in **Fig. 3a-d**, Pb-vacancy (V_{Pb}) on (100) surfaces is one potential defect type that has been shown in the bulk, leading to shallow levels near the valence band maximum (VBM), resulting in undesirable charge accumulation and potential recombination at the perovskite-PCBM interface. However, the projected density of states (pDOS) obtained from DFT simulations (PAW PBE-GGA) on a 2×2×4 perovskite slab with a PCBM molecule on the most commonly exposed (100) facet do

not show detrimental electronic states for either charged or neutral V_{Pb} defects. The carbon p-states (C, p) of the PCBM are well aligned to receive carriers from the perovskites. The iodine p-levels that define the perovskite's VBM do not encroach on the Carbon p-levels for the relatively large concentration of V_{Pb} simulated (25% atomic V_{Pb}/Pb), implying the perovskite is free of hole traps at the surface for this defect type. Second, it was found that the peaks of Pb *4f* (**Fig. 3e**), I *3d* (**Fig. 3e**) and Cs *3d/5* (Fig. S13) shifted towards a lower binding energy level in $CsPbI_3$ QDs of the hybrid film, suggesting the formation of coordination bonds between carboxyl moieties and mostly under-coordinated Pb^{2+} ions on QD surfaces. The systematic characterizations of the hybrid QD blend film indicate the improved carrier dynamic process and molecular interaction. As illustrated in **Fig. 3f,** when PCBM blends with $CsPbI_3$ QDs at the optimal ratio, the spherically symmetric C_{60} facilitates the efficient charge transfer at the interfaces. In addition, one problem with the conventional $CsPbI_3$ QD film after the process of ligand removal is its sensitivity to moisture. The addition of hydrophobic PCBM could not only reduce the QD boundaries but also passivate the QD surfaces via forming strong bonding of the carboxyl group with the under-coordinated Pb^{2+} ions on the QD surfaces.

Moreover, the top-view SEM images in Fig. S14 clearly exhibit very similar morphology in the control and hybrid films, showing that both films are dense with similar surface roughness. Atomic force microscopy (AFM) height images in Fig. S15 indicate that the hybrid film is smoother than the control one. Both films have similar surface topography with roughness of 7.3 nm for the control film and 7.1 nm for the hybrid film, suggesting that the PCBM addition did not significantly alter the QD film morphology.

Flexible QD photovoltaics

To explore the advantageous of HIA strategy in fabricating efficient QD flexible solar cells, we fabricated perovskite QD flexible solar cells with same structure for rigid device using conventional PET (polyethylene terephthalate)/ITO substrates. **Fig. 4a** and **Table 1** presents the optimized *J-V* characteristics and PCE distribution of the control and target flexible devices, both the efficiency and device reproducibility are significantly improved using HIA modification, with a record PCE of 12.3%, greatly outperforming both control and previous reports (Table S2). What is more exciting is that this HIA strategy enables us to practically demonstrate the better suitability of the perovskite QDs on flexible photovoltaics compared to extensively studied thin-film materials[46-48]. **Fig. 4b** shows the performance comparison between all-inorganic $CsPbI_2Br$ perovskite bulk film and QD device. It should be noted that the preparation of all-inorganic $CsPbI_3$ bulk film needs high-temperature (>320 ^oC) annealing process[49-50], which will damage the PET flexible substrate. Therefore, we select $CsPbI_2Br$ with decreased phase transition temperature down to ~100 ^oC. As shown in **Fig. 4b**, after 100 bending cycles at the radius of 0.75 cm, the efficiency of QD devices decreased to 90% of the initial value that may be attributed to the degradation of the rigid electrode ITO or Ag contact,[51] while only ~75% of initial efficiency was remained for the $CsPbI_2Br$ thin-film based device. The detailed device parameters, i.e., open-circuit voltage (V_{oc}), J_{sc},

and fill factor (FF) for $CsPbI_3$ QD and $CsPbI_2Br$ thin film devices are shown in Fig. S16. These results first indicate the superior performance in QD-based flexible devices relative to its bulk thin-film counterpart.

To further investigate the degradation of device performance and understand the internal stress in films after bending, we carried out the film mechanical durability (**Fig. 4c**) test using SEM examination on a variety of materials ($CsPbI_3$ QD, PbS QD, $CsPbI_2Br$ thin-film, and $Cs_{0.05}MA_{0.85}MA_{0.1}PbI_{2.55}Br_{0.45}$ mixed perovskite thin-film) deposited on the same flexible PET/ITO substrate, as shown in Fig. S17. We don't observe any apparent surface morphology change after bending up to 1000 times in both $CsPbI_3$ (**Fig. 4d**) and PbS (**Fig. 4e**) QD films. However, crystal cracks propagation is apparently noticeable in the $CsPbI_2Br$ thin-film after 100 times bending, and gradually grow up to micrometer scale when further increasing the bending cycles (**Fig. 4f**). Similar trend was found that huge cracks and even severe crystal shedding appeared after 1000 cycle bending in the mixed perovskite thin-film with large crystal grains (**Fig. 4g**). These results allow us to conclude that QD films possess much better mechanical durability than bulk film since the intrinsic nanoscale boundaries and soft surface ligands in the low-dimensional QD materials are beneficial for releasing the thin film internal stress, as described in **Fig. 4c**. Based on the more durable performance of QD device, this is the first time to experimentally prove that QDs potentially offer higher mechanical flexibility than thin-film materials, and displaying their prominence in flexible devices.

Conclusion

In summary, by developing a simple yet efficient HIA strategy, we have demonstrated high-efficiency and flexible $CsPbI_3$ QD solar cells for the first time. The introduction of organic molecule PCBM into the $CsPbI_3$ QD layer leads to the formation of a hybrid heterojunction interfacial connecting layer, which plays an important role in enhancing the QD film quality and improving the contact between the active layer and the ETL. The homogeneous modification of PCBM within QD layer can strengthen charge transfer at both QD heterointerfaces and QD/ETL interfaces as well as suppress interfacial recombination, which are key factors governing the device efficiency. Consequently, the HIA strategy enabled us to realize $CsPbI_3$ QD solar cells with a highest efficiency of 15.1%, with ~25% improvement compared to the control one. More importantly, we also obtained the first flexible perovskite QD solar cells, recording a PCE of 12.3% assisted by the HIA strategy, as well as improved mechanical flexibility relative to its thin-film counterpart. Armed with all these results, we believe that the work demonstrated here offers a new route to improving the performance of QD photovoltaic devices and the strategy may be generalized to advance other QD-based optoelectronics.

Methods

Materials

Lead iodide (PbI_2, 99.999%, Aldrich), Cesium carbonate (Cs_2CO_3, 99%, Aldrich), octadecene (ODE, 90%, Aldrich), oleic acid (OA, 90%, Aldrich), oleylamine (OLA, Aldrich, 70%), hexane (anhydrous, 95%, Sigma), octane (anhydrous, ≥99%, Sigma), methyl acetate (MeOAc, anhydrous, 99.5%, Sigma), chlorobenzene (CB, anhydrous, 99.8%, Sigma), PCBM (>99.9, Sigma), and tin(IV) oxide (SnO_2, 15% in H_2O colloidal dispersion, Alfa Aesar) were used as received without further purification unless mentioned. Glass/ITO and PET/ITO were purchased from the Zhuhai Kaivo Optoelectronic Technology Co. Ltd. $CsPbI_2Br$ thin-film devices were prepared according to reported methods[52]. PbS QD films were fabricated according to the reported methods[15] and mixed perovskite thin-film were prepared according to reported methods[48].

Characterizations

The current density-voltage characteristics of devices were measured using Keithley 2400 (I-V) digital source meter under a simulated AM 1.5G solar irradiation at 100 mW/cm2 (Newport, AAA solar simulator, 94023A-U). The external quantum efficiency spectra were recorded through certified EQE equipment. The PL spectra measurements were performed at room temperature by a homemade laser PL spectroscopy system (Crystal Laser, Model BLC-050-405). The laser pulse width was 130 fs, and the repetition rate was 100 M Hz. The excitation wavelength for both PL and TRPL measurements is 600 nm. Scanning electron microscope (SEM) measurements were carried out by using a FEI Nova Nano SEM 450. Transmission electron micrcoscope (TEM) measurements were performed by a JEOL JEM-2010 and JEOL JEM-F200 operated at 200 kV. UV−vis absorption spectra were obtained using U-4100 spectrophotometer (Hitachi). Fourier transform infrared spectroscopy (FTIR) was performed on a Thermo Fisher FTIR6700. X-ray photoelectron spectroscopy (XPS) and ultra-violet photoelectron spectroscopy (UPS) measurements were conducted by a VG ESCALAB MK2 system with monochromatized Al Kα radiation under a pressure of 5.0 × 10^{-7} Pa. Contact angle measurements were conducted by a Data physics OCA-20 system at room temperature in ambient atmosphere. The TA measurements were carried out under ambient conditions, the fs-TA measurements were performed on a Helios pump-probe system (Ultrafast Systems LLC) combined with an amplified femtosecond laser system (Coherent).

$CsPbI_3$ QD synthesis and purification

1 g PbI_2, 5 ml oleylamine and 50 ml 1-octadecene were added into 250 ml three-neck flask and under vacuum for 60 min at 110 °C. The flask was then filled with N_2 and heated under protection by N_2 flow. When the temperature reaches 165 °C, 8 mL Cs-oleate[32] (0.0625 M) precursor was swiftly injected into the reaction mixture. The mixture became dark red rapidly, and after 5 s the reaction was quenched by an ice bath. During the purification process, cubic-phase QDs were extracted by anhydrous MeOAc. Firstly, the synthesized $CsPbI_3$ QDs were separated into eight parts and each one precipitated by adding 24 mL MeOAc (ratio of QD reaction solution: MeOAc is 1:3), then centrifuged at 8,000 rpm for 5 min. The precipitation in each centrifuge tube was re-dispersed in 3 mL hexane, precipitated again with 2-fold volume MeOAc (6 mL) and centrifuged at 10,000 rpm for 5 min. The QDs were then re-dispersed in 20 mL hexane total and centrifuged again at 4 000 rpm for 5 min to remove excess PbI_2 and Cs-oleate. The

supernate was kept at 4 °C for 12 h in the dark to precipitate excess Cs-oleate and Pb-oleate. After cooling subsidence, the QD solution needs to be centrifuged again at 4,000 rpm for 5 min to obtain the final product. The final product was dry by N_2 gas and re-dispersed into octane and chlorobenzene with a concentration of 70 mg/ml for each. PCBM was added into $CsPbI_3$ QD chlorobenzene solution to prepare hybrid solution with the PCBM: $CsPbI_3$ ratio being 5 mg/ml:70 mg/ml under stirring in N_2 filled glovebox.

$CsPbI_3$ QD solar cell fabrication

The SnO_2 nanoparticle solution with a diluted weight concentration of 2.5% was spin-coated on onto pre-patterned ITO glass substrates and annealed at 120 °C for 30 min in ambient condition. Then the SnO_2 film was treated with O_2 plasma for 2 min before following layers would be deposited. For the control device fabrication, an ultra-thin PCBM layer was prepared by spin-coating PCBM CB solution (5 mg/ml) at 5000 RPM for 30 s. $CsPbI_3$ QD layer (70 mg/mL in octane) or PCBM/$CsPbI_3$ QD (5 mg/mL/70 mg/mL in CB) layers were deposited by spin-coating at 1000 RPM for 30 s, treated with pure anhydrous MeOAc for 20 s. The total thickness was control by varying deposited layers. 20 mg/ml PTB7 solution was spin-coated atop QD films as HTLs. Finally, 10 nm MoO_3 and 100 nm Ag electrode were prepared by thermal evaporation. For the target device fabrication, hybrid buffer solution was spin-coated on SnO_2 layer, treated with anhydrous MeOAc. The total thickness was control by varying deposited layers of hybrid and pure QD layers. The other layers were prepared by using the identical recipe with those of control device. For the flexible device fabrication: SnO_2 NP solution was spin-coated on O_2 plasma treated ITO/PET substrates and annealed on 120 °C for 30 min in ambient condition. Other layers were fabricated by using the identical recipe with that of target device.

Declarations

Acknowledgments

Author Contributions

J.Y., J.M.L. and T.W. conceived and supervised the project; L.H. did most the experimental work. Q.Z., S.H, J.Z., L.S., C.-H.L. and A.W.Y.H. contributed the data collection, analysis and discussion. X.G. and Y.K. synthesized the perovskite QDs. R. P. did the DFT simulation. Q.L. and T.W. did optical characterizations. S.C. and R.D.T. did TEM and SEM measurements. The manuscript was drafted and revised by L.H., J.Y. and T.W. with input from all authors.

Competing interests:

The authors declare no competing interests.

Additional information

Supplementary information is available in the online version of the paper. Reprints and permissions information is available online at www.nature.com/reprints.

References

1. Tang J, *et al.* Colloidal-quantum-dot photovoltaics using atomic-ligand passivation. *Nat. Mater.* 10, 765–771 (2011).

2. Ning Z, *et al.* All-inorganic colloidal quantum dot photovoltaics employing solution-phase halide passivation. *Adv. Mater.* 24, 6295–6299 (2012).

3. Stavrinadis A, *et al.* Heterovalent cation substitutional doping for quantum dot homojunction solar cells. *Nat. Commun.* 4, 2981 (2013).

4. Zhitomirsky D, *et al.* Engineering colloidal quantum dot solids within and beyond the mobility-invariant regime. *Nat. Commun.* 5, 3803 (2014).

5. Hu L, *et al.* Graphene doping improved device performance of ZnMgO/PbS colloidal quantum dot photovoltaics. *Adv. Funct.Mater.* 26, 1899–1907 (2016).

6. Yang Z, *et al.* Mixed-quantum-dot solar cells. *Nat. Commun.* 8, 1325 (2017).

7. Song JH, Choi H, Pham HT, Jeong S. Energy level tuned indium arsenide colloidal quantum dot films for efficient photovoltaics. *Nat. Commun.*9, 1–9 (2018).

8. Wang Y, *et al.* Room-temperature direct synthesis of semi-conductive PbS nanocrystal inks for optoelectronic applications. *Nature communications* 10, 4267 (2019).

9. Konstantatos G, *et al.* Hybrid graphene–quantum dot phototransistors with ultrahigh gain. *Nat. Nano.* 7, 363–368 (2012).

10. Nikitskiy I, *et al.* Integrating an electrically active colloidal quantum dot photodiode with a graphene phototransistor. *Nat. Commun.*7, 11954 (2016).

11. Ren Z, *et al.* Bilayer PbS Quantum Dots for High-Performance Photodetectors. *Adv. Mater.* 29, 1702055 (2017).

12. Livache C, *et al.* A colloidal quantum dot infrared photodetector and its use for intraband detection. *Nat. Commun.* 10, 2125 (2019).

13. Sun L, *et al.* Bright infrared quantum-dot light-emitting diodes through inter-dot spacing control. *Nat. Nano.* 7, 369–373 (2012).

14. Shirasaki Y, Supran GJ, Bawendi MG, Bulović V. Emergence of colloidal quantum-dot light-emitting technologies. *Nat. Photon.* 7, 13–23 (2013).

15. Liu M, *et al.* Hybrid organic–inorganic inks flatten the energy landscape in colloidal quantum dot solids. *Nat. Mater.* 16, 258–263 (2017).

16. Zhang Z, *et al.* A New Passivation Route Leading to Over 8% Efficient PbSe Quantum-Dot Solar Cells via Direct Ion Exchange with Perovskite Nanocrystals. *Adv. Mater.* 29, 1703214 (2017).

17. Wang R, *et al.* Highly efficient inverted structural quantum dot solar cells. *Advanced Materials* 30, 1704882 (2018).

18. Sun B, *et al.* Monolayer Perovskite Bridges Enable Strong Quantum Dot Coupling for Efficient Solar Cells. *Joule*, (2020).

19. Swarnkar A, *et al.* Quantum dot–induced phase stabilization of α-CsPbI3 perovskite for high-efficiency photovoltaics. *Science* 354, 92–95 (2016).

20. Sanehira EM, *et al.* Enhanced mobility CsPbI3 quantum dot arrays for record-efficiency, high-voltage photovoltaic cells. *Sci. Adv.* 3, eaao4204 (2017).

21. Yuan J, *et al.* Band-aligned polymeric hole transport materials for extremely low energy loss α-CsPbI3 perovskite nanocrystal solar cells. *Joule* 2, 2450–2463 (2018).

22. Zhao Q, *et al.* High efficiency perovskite quantum dot solar cells with charge separating heterostructure. *Nat. Commun.* 10, 2842 (2019).

23. Ling X, *et al.* Guanidinium-Assisted Surface Matrix Engineering for Highly Efficient Perovskite Quantum Dot Photovoltaics. *Adv. Mater.* 32, 2001906 (2020).

24. Wang Y, *et al.* Surface Ligand Management Aided by a Secondary Amine Enables Increased Synthesis Yield of $CsPbI_3$ Perovskite Quantum Dots and High Photovoltaic Performance. *Adv. Mater.* 32, 2000449 (2020).

25. Xue J, *et al.* Surface ligand management for stable FAPbI3 perovskite quantum dot solar cells. *Joule* 2, 1866–1878 (2018).

26. Ling X, *et al.* 14.1% CsPbI3 perovskite quantum dot solar cells via cesium cation passivation. *Adv. Energy Mater.* 9, 1900721 (2019).

27. Yuan J, *et al.* Metal Halide Perovskites in Quantum Dot Solar Cells: Progress and Prospects. *Joule* 4, 1160–1185 (2020).

28. Hao M, *et al.* Ligand-assisted cation-exchange engineering for high-efficiency colloidal $Cs_{1-x}FA_xPbI_3$ quantum dot solar cells with reduced phase segregation. *Nat. Energy* 5, 79–88 (2020).

29. Hazarika A, *et al.* Perovskite quantum dot photovoltaic materials beyond the reach of thin films: full-range tuning of A-site cation composition. *ACS Nano* 12, 10327–10337 (2018).

30. Zhang X, Hägglund C, Johansson EM. Highly efficient, transparent and stable semitransparent colloidal quantum dot solar cells: a combined numerical modeling and experimental approach. *Energy Environ. Sci.* 10, 216–224 (2017).

31. Cho Y, *et al.* Charge transport modulation of a flexible quantum dot solar cell using a piezoelectric effect. *Adv. Energy Mater.* 8, 1700809 (2018).

32. Li F, *et al.* Perovskite Quantum Dot Solar Cells with 15.6% Efficiency and Improved Stability Enabled by an α-CsPbI3/FAPbI3 Bilayer Structure. *ACS Energy Lett.* 4, 2571−2578 (2019).

33. YousefiAmin A, *et al.* Fully Printed Infrared Photodetectors from PbS Nanocrystals with Perovskite Ligands. *ACS Nano* 13, 2389−2397 (2019).

34. Yuan J, *et al.* Spray-Coated Colloidal Perovskite Quantum Dot Films for Highly Efficient Solar Cells. *Adv. Funct. Mater.* 29, 1906615 (2019).

35. Liu H, *et al.* Physically flexible, rapid-response gas sensor based on colloidal quantum dot solids. *Adv. Mater.* 26, 2718−2724 (2014).

36. Choi MK, Yang J, Hyeon T, Kim D-H. Flexible quantum dot light-emitting diodes for next-generation displays. *npj Flexible Electronics* 2, 1−14 (2018).

37. Zhang X, Santra PK, Tian L, Johansson MB, Rensmo Hk, Johansson EM. Highly efficient flexible quantum dot solar cells with improved electron extraction using MgZnO nanocrystals. *ACS Nano* 11, 8478−8487 (2017).

38. Zhang X, Öberg VA, Du J, Liu J, Johansson EM. Extremely lightweight and ultra-flexible infrared light-converting quantum dot solar cells with high power-per-weight output using a solution-processed bending durable silver nanowire-based electrode. *Energy Environ. Sci.* 11, 354−364 (2018).

39. Jung HS, Han GS, Park N-G, Ko MJ. Flexible perovskite solar cells. *Joule* 3, 1850−1880 (2019).

40. Fukuda K, Yu K, Someya T. The Future of Flexible Organic Solar Cells. *Adv. Energy Mater.* 10, 2000765 (2020).

41. Xue J, *et al.* A Small-Molecule "Charge Driver" enables Perovskite Quantum Dot Solar Cells with Efficiency Approaching 13%. *Adv. Mater.* 31, 1900111 (2019).

42. Ding C, *et al.* Photoexcited hot and cold electron and hole dynamics at $FAPbI_3$ perovskite quantum dots/metal oxide heterojunctions used for stable perovskite quantum dot solar cells. *Nano Energy* 67, 104267 (2020).

43. Lu K, *et al.* High-Efficiency PbS Quantum-Dot Solar Cells with Greatly Simplified Fabrication Processing via "Solvent-Curing". *Adv. Mater.* 30, 1707572 (2018).

44. Stavrinadis A, Pradhan S, Papagiorgis P, Itskos G, Konstantatos G. Suppressing deep traps in PbS colloidal quantum dots via facile iodide substitutional doping for solar cells with efficiency > 10%. *ACS Energy lett.* 2, 739−744 (2017).

45. High Efficiency Mesoscopic Solar Cells Using $CsPbI_3$ Perovskite
Chen K., *et al.* High Efficiency Mesoscopic Solar Cells Using $CsPbI_3$ Perovskite Quantum Dots Enabled by Chemical Interface Engineering. *J. Am. Chem. Soc.* 142, 3775−3783 (2020)

46. Tan H, *et al.* Efficient and stable solution-processed planar perovskite solar cells via contact passivation. *Science* 355, 722−726 (2017).

47. Yang S, *et al.* Stabilizing halide perovskite surfaces for solar cell operation with wide-bandgap lead oxysalts. *Science* 365, 473−478 (2019).

48. Shi L, *et al.* Gas chromatography–mass spectrometry analyses of encapsulated stable perovskite solar cells. *Science 368*, eaba2412 (2020).

49. Wang Q, Zheng X, Deng Y, Zhao J, Chen Z, Huang J. Stabilizing the α-phase of $CsPbI_3$ perovskite by sulfobetaine zwitterions in one-step spin-coating films. *Joule* 1, 371–382 (2017).

50. Li B, *et al.* Surface passivation engineering strategy to fully-inorganic cubic $CsPbI_3$ perovskites for high-performance solar cells. *Nat. Commun.* 9, 1076 (2018).

51. Wang C, *et al.* Water vapor treatment of low-temperature deposited SnO_2 electron selective layers for efficient flexible perovskite solar cells. *ACS Energy Lett.* 2, 2118–2124 (2017).

52. Wang Y, *et al.* Dual Interfacial Engineering Enables Efficient and Reproducible $CsPbI_2Br$ All-Inorganic Perovskite Solar Cells. *ACS Appl. Mater. Interfaces 12*, 31659–31666 (2020).

Tables

Table 1. Statistics of $CsPbI_3$ QD solar cell performance with varied QD absorber layers based on 24 devices.

Substrate	Device structure	V_{oc} (V)	J_{sc} (mA•cm^{-2})	FF	PCE (%)
Glass/ITO (Rigid)	Control	1.23 (1.22±0.02)	13.6 (13.3±0.7)	0.74 (0.73±0.02)	12.4 (11.9±0.4)
	Target	1.26 (1.24±0.03)	15.2 (14.4±0.9)	0.78 (0.76±0.03)	15.1 (14.6±0.6)
PET/ITO (Flexible)	Control	1.16 (1.11 ± 0.06)	12.0 (11.5 ± 1.6)	0.70 (0.67 ± 0.06)	9.7 (8.5 ± 0.6)
	Target	1.24 (1.19 ± 0.04)	13.6 (13.1 ± 1.2)	0.73 (0.72 ± 0.05)	12.3 (11.3 ± 0.4)

Figures

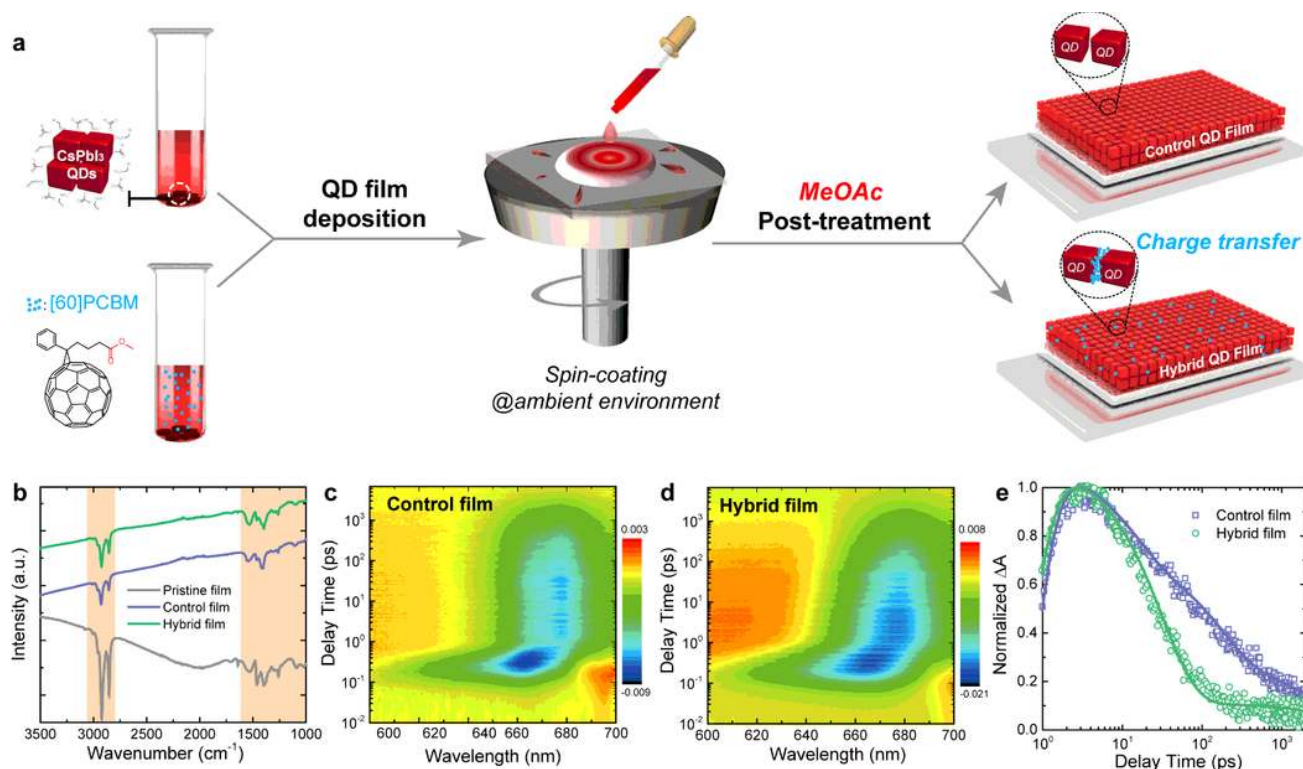**Figure 1**

The preparation and properties of CsPbI3 QD and CsPbI3 QD/PCBM films. a Schematic of the fabrication of pristine, control and hybrid CsPbI3 QD films. b FTIR spectra of pristine, control and hybrid films on SnO2/ITO glass substrates (characteristic peaks of organic species are highlighted by the red background). c-d 2D time-wavelength-dependent TA color maps of the control and the hybrid CsPbI3 QD films excited at 600 nm. e Normalized TA dynamics of the ground-state bleach (GSB) for control and hybrid CsPbI3 QD films. For the control film, the components are $\tau_1=1.3$ ps, $\tau_2=52.3$ ps and $\tau_3=483.2$ ps. For the hybrid film, the time components are extracted as $\tau_1=1.4$ ps, $\tau_2=57.6$ ps and $\tau_3=312.8$ ps.
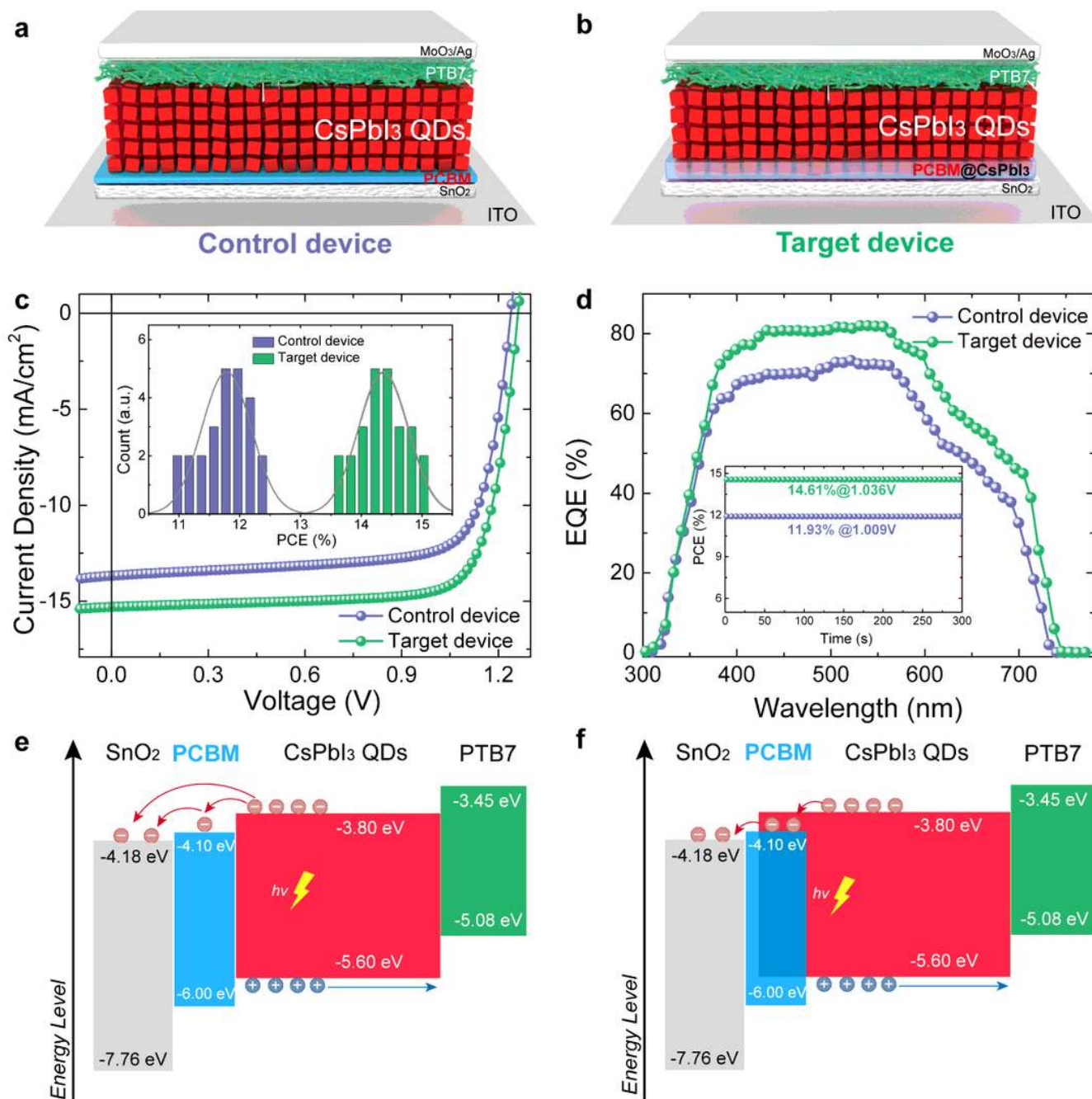
Figure 2

Photovoltaic performance of solar cells. a-b Schematic diagram of the control device and target device. c J-V curves measured under AM 1.5G solar irradiation at 100 mW/cm2 (inset: PCE distribution of control and target devices). d EQE curves of control and target devices (inset: stabilized power output of control and target devices). e-f Band energy level diagram of control and target devices.
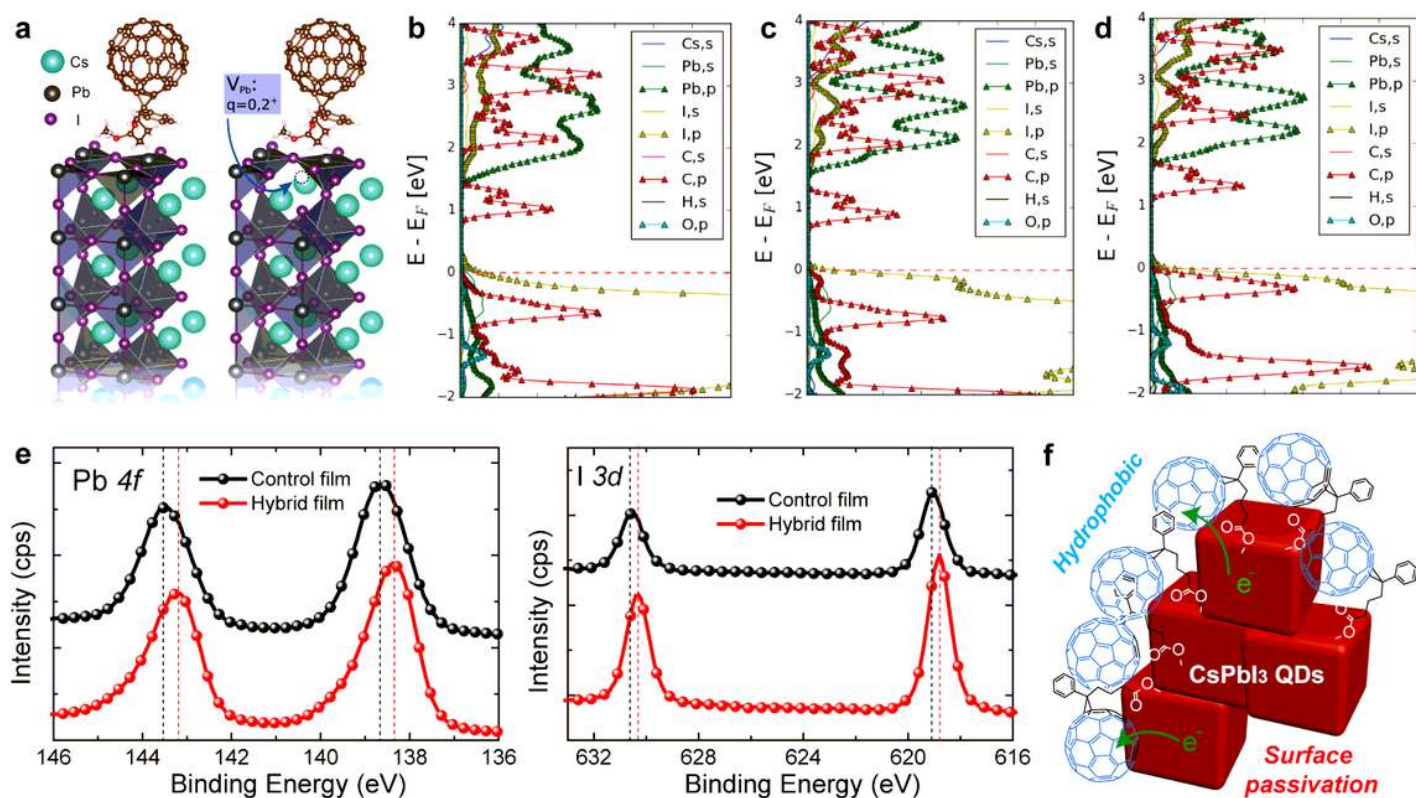
Figure 3

Molecular interaction between QD and PCBM. a Schematic diagrams of the simulated unit cell, showing the perovskite slab system with and without a charged Pb vacancy defect. b-d The electronic pDOS for three cases: without Pb vacancy, with a neutral and with a Pb vacancy carrying a formal 2+ charge. e XPS signals of Pb 4f and I 3d in the control and the hybrid films. f Schematic diagram of the hydrophobic PCBM passivating surface of CsPbI3 QDs.
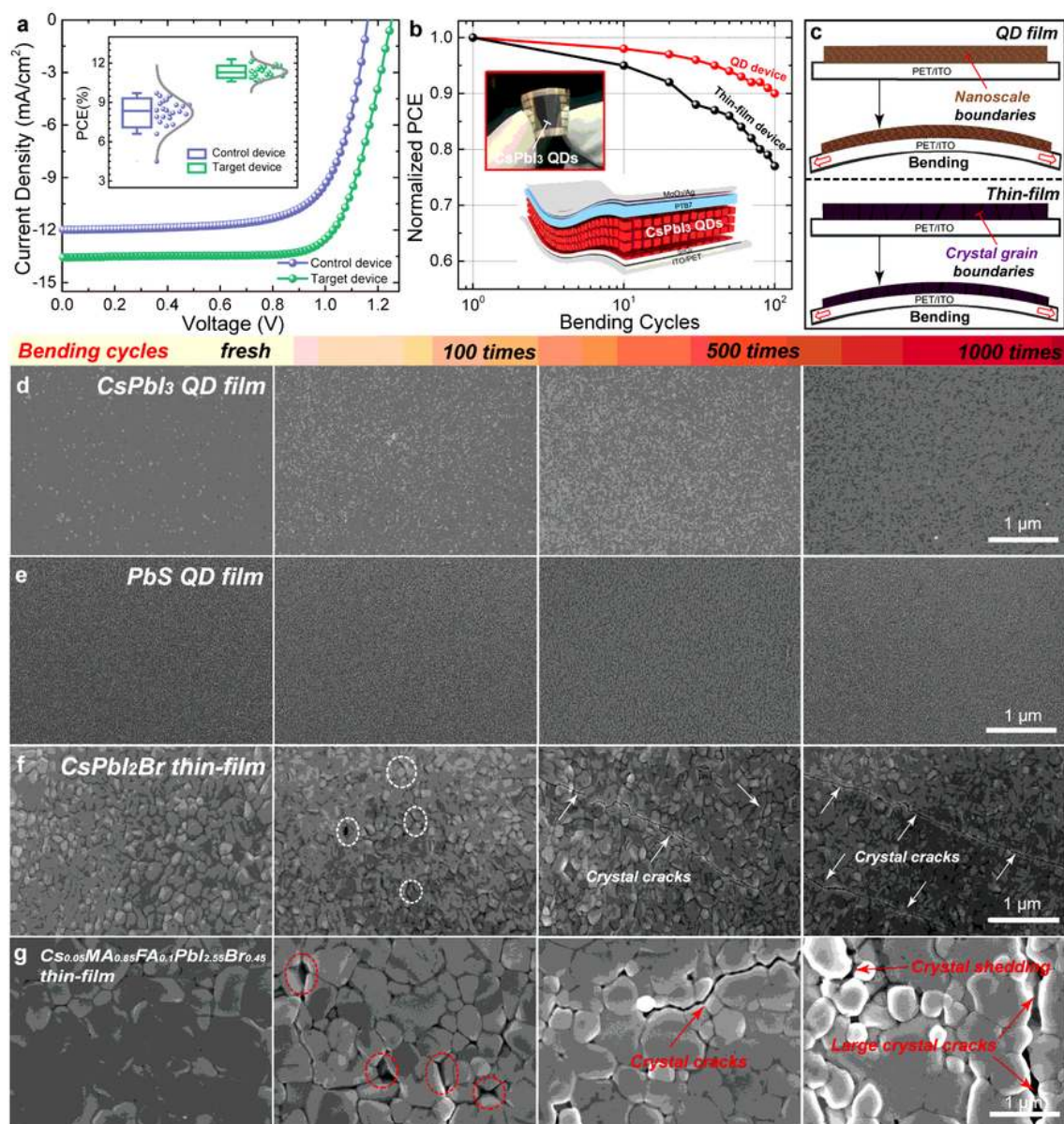
Figure 4

Flexible solar cells and mechanical stability. a J-V curves of the flexible champion device measured under AM 1.5G solar irradiation at 100 mW/cm2 (Inset: schematic diagram of flexible device architecture and PCE distribution of the flexible devices). b PCE of CsPbI3 QD solar cell and CsPbI2Br thin-film solar cell as a function of bending cycles (Inset: photograph of the flexible QD solar cell). c Schematic diagram of the bending mechanical testing of QD and thin-film on flexible substrate. d-g Top-view SEM images of the

CsPbI3 QD film, PbS QD film, CsPbI2Br and mixed perovskite thin-film fabricated on PET/ITO (2.5×2.5 cm) with mechanical bending (curvature radius of 0.75 cm).

Supplementary Files

This is a list of supplementary files associated with this preprint. Click to download.

- FlexiblePVSKQDSCsSI.docx